

RESEARCH

Open Access



Flow-through experiments on the interaction of sandstone with Ba-rich fluids at geothermal conditions

Pia Orywall^{1,2*} , Kirsten Drüppel³, Dietmar Kuhn¹, Thomas Kohl⁴, Michael Zimmermann⁵ and Elisabeth Eiche⁶

*Correspondence: pia.orywall@kit.edu; p.orywall@rbs-wave.de

¹ Institute of Nuclear and Energy Technology, Karlsruhe Institute of Technology, Herrmann-von Helmholtz-Platz 1, 76344 Eggenstein-Leopoldshafen, Germany

Full list of author information is available at the end of the article

Abstract

It is commonly known that heat extraction and decompression can lead to mineral precipitation and reservoir clogging in geothermal systems. In the Upper Rhine Graben, the precipitating minerals are mainly barite and calcite. This study focuses on clogging processes due to mineral precipitation in porous reservoir rocks, i.e., sandstone. The goal is to develop, build, and put into operation the HydRA apparatus, a facility for performing experiments on forced precipitation of barite in the pore spaces of sandstone under geothermally relevant pressure and temperature conditions. Barite precipitation during the flow-through is provoked by using barite-supersaturated solutions with a saturation index (SI) of 1.75. Scanning electron microscopy (SEM) investigations are used to detect barite crystal agglomerations and clogging of the pore spaces by overgrowths on these agglomerates. Following this, different crystal shapes are observed. The results are confirmed by permeability analyses before and after the flow-through experiments. Comparison of the major and trace element compositions of the original and reacted sandstones indicates element mobility due to water–rock interaction, even during the short-time experimental runs (max. 24 h).

Keywords: Flow-through experiments, Percolation, Barite, Precipitation, Dissolution, Water–rock interactions, Geothermal energy, Permeability, Pore space clogging

Background

When heat is extracted from geothermal fluids, the chemical equilibrium in the geothermal system is changed and thus some mineral phases become supersaturated and precipitate. Depending on the origin of the fluid and the degree of cooling, the main precipitating mineral phases observed are carbonates (CaCO_3), sulfates (CaSO_4 , BaSO_4 , SrSO_4), silica, and sulfides (FeS , PbS , CuS) (Stober and Bucher 2012). During a geothermal cycle, this modified fluid is re-injected into the reservoir and thus may change the mineralogical composition of the rock drastically. Dissolution of minerals may alter the rock structure, whereas precipitation of mineral phases from the fluid may have an effect on the permeability.

Flow-through experiments with sandstones were performed in numerous studies with regard to geothermal energy use for heat storage, energy extraction, or CO_2 -storage. In all these studies, a fluid is forced to flow through reservoir rocks, like limestone,

crystalline rocks, or sandstones. Investigations on formation damages due to particle redistribution in sandstone reservoirs were performed and the existence of a critical flow rate was confirmed by Ochi and Vernoux (1998). Rosenbrand et al. (2015) attributed the reduction of the permeability of reacted sandstones to the migration of fine particles, depending on the salinity of the percolating fluid and temperature. Another study shows that the decrease in permeability of kaolinite containing sandstones is related to the dissolution and re-precipitation of the kaolinite (Rosenbrand et al. 2014).

By performing experiments with oxidized water at the geothermal site of Neustadt-Glewe, Kühn et al. (1998) showed that a decrease of the permeability is caused by the precipitation of Fe-hydroxides and/or particle redistribution. Research work on water-rock interaction of granite was performed by Savage et al. (1992), implying that temperature, flow rate, and fluid composition are crucial parameters which determine the progress of the chemical reactions and hydraulic changes of the rock. Banks et al. (2014) present an experimental design for predicting the scaling risks concerning barite mineralization in basin-hosted enhanced geothermal systems.

In geothermal exploration and the following energy production, barite supersaturation and precipitation is caused by extracting the heat from a reservoir fluid, which is supersaturated or slightly undersaturated with regard to barite (Pauwels et al. 1993). Either barite particles nucleate from the fluid and clog the pore gussets or precipitation occurs in the available pore space by overgrowing matrix particles. One good example is Soultz-sous-Forêts (France), where geothermal heat extraction leads to massive barite deposits in the tube on the reinjection side (Scheiber et al. 2014). The influence of rising temperature is studied by investigations on barite in a closed system. Compared to ambient temperature, barite precipitation rates are increasing with decreasing temperatures (Blount 1977).

Christy and Putnis (1993) studied barite precipitation and dissolution in barite-supersaturated NaCl brines at temperatures of up to 85 °C. They state that the growth and dissolution of barite is not sensitive to the pH value and NaCl concentration and that the barite precipitation follows second-order kinetics. In a more recent study, however, the influence of the pH of the solution was demonstrated in nanoscale experiments. Under alkaline pH-conditions, barite growth stopped during progressive precipitation suggesting a distortion of the barite structure, which may be caused by the $\text{OH}^-/\text{CO}_3^{2-}$ ions of the alkaline solution. At high pH values, a smaller particle size of barite was observed (Ruiz-Agudo et al. 2015).

In the present work, the barite precipitation in porous sandstone is studied. A special experimental setup is designed to simulate realistic geothermal reservoir conditions. A flow-through apparatus is used for the experiments, in which an artificial geothermal fluid is forced through a common sandstone of the Upper Rhine Graben. The experiments are carried out at elevated temperatures of up to 150 °C and pressure ranges of up to 300 bar with a fixed flow rate of 2 cm³/min. These experimental parameters are closely aligned to the operational parameters of geothermal sites in the Upper Rhine Graben, as for instance, Soultz-sous-Forêts (France) and Bruchsal (Germany) (Herzberger et al. 2010; Genter et al. 2010). In the experiments, an artificial fluid with a well-defined supersaturation of barite (SI 1.75) is used. This composition is similar to the composition of the natural fluid of Soultz-sous-Forêts (Sanjuan et al. 2010).

The results of this study provide information on the processes and the risks of pore space clogging related to barite precipitation at geothermal sites and help to specify the effects of the reinjection of a chemically modified geothermal fluid into the reservoir, particularly with respect to the permeability change of the reservoir formation.

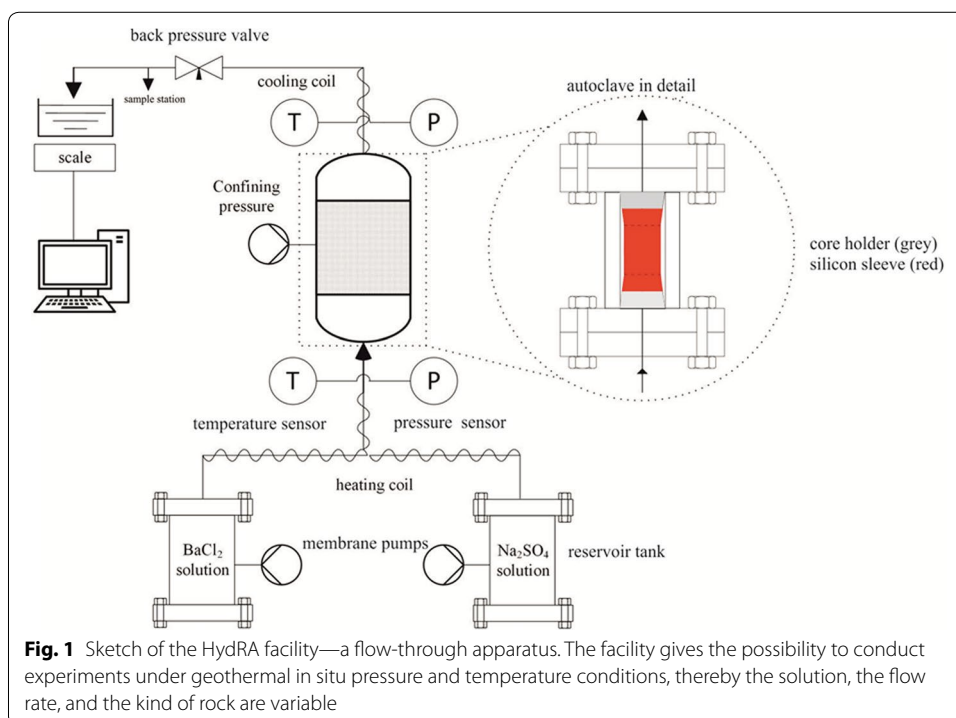
Methods

Experimental apparatus and procedure

All experiments were performed in HydRA (hydrothermal reaction apparatus), in which rock samples are percolated at a fixed flow rate under geothermally relevant temperature and pressure conditions by a barite-supersaturated fluid to induce barite precipitation. HydRA is designed and constructed exclusively for this kind of experiments by the Department of Energy and Process Engineering (Institute of Nuclear and Energy Technologies) at the Karlsruhe Institute of Technology (KIT).

The centerpiece of HydRA (Fig. 1) is the autoclave in which the rock sample is mounted. It is suitable for cylindrical samples with the dimensions of 50.8 mm × 25.4 mm. Temperatures of up to 150 °C and pressures of up to 350 bar can be used as boundary conditions in the experiments. Flow rates can be adjusted in a range of 2–20 cm³/min.

Further main components of HydRA are two reservoir tanks for the hydrochemical solutions, three pumps (LEWA membrane pumps), the hydrochemical sampling point, a scale, a heater, and two pressure and two temperature sensors. All components are connected by steel pipes (Herfurth and Orywall 2015). The pipes, the autoclave, and the reservoir tanks are made from non-corrosive austenitic steel (DIN EN 10088-3 2014) 1.4571 with the following composition of the main elements: Fe 66.7 wt %, Cr 16.7 wt %, and Ni 10.72 wt %. The steel can be used up to temperatures of 550 °C.



The rock sample is fixed in a sample holder (Fig. 1) and tightly enclosed by a silicon tube (Fig. 1, red marked) with a wall thickness of 3 mm. To avoid a flow between this silicon tube and the sample, a confining pressure, which is always 10% higher than the pressure in the percolation system, is applied, using a separate pump and a closed water cycle with distilled water.

To fit into the autoclave, the cylindrical rock sample has to have a length of 50.8 mm and a diameter of 25.4 mm. The length of the sample has to be precisely adhered to fit into the core holder of the autoclave. The samples used were homogeneous, without any visible layering or damages at the edges of the rock body. The sandstones were dried under ambient conditions in a hood (protected in a glass bowl) until their weight was constant.

The fluid, which is pumped through the sample, circulates in a separate cycle. Reservoir tank 1 mainly contains the solution of a background electrolyte with barium chloride (BaCl_2), whereas reservoir tank 2 contains a solution of the background electrolyte with potassium sulfate (Na_2SO_4). The choice of the background electrolyte is based on two considerations: (1) the composition of the solution should be as close as possible to the natural fluid of the Upper Rhine Graben and (2) the supersaturated mineral phases should not precipitate immediately after mixing (Canic et al. 2015; Kaufmann-Knoke 1992). The two solutions are mixed at the entry of the rock sample. The flow rate of the solutions is adjusted via two pumps, one for each reservoir tank. Both pumps have an individual water cycle which is filled with distilled water. This design separates the technical equipment of the pumps from the saline solution and thus avoids corrosion.

After leaving the rock sample, the solution is conducted through a heat exchanger that cools down the hot percolated fluid. Behind this, a back pressure valve is installed to control the pressure in the system. At the exit of the apparatus, the flow quantity of the solution is measured using a scale and fluid samples are collected (Fig. 1).

All system data (temperatures, pressures, and mass flows) are recorded digitally with the software OPAL (Daubner and Krieger 2010). The apparatus is controlled using a Siemens programmable logic control (PLC) in which also safety functions are implemented. If, for example, the temperature of the heating system or the differential pressure exceeds the permitted range (all values are monitored by the PLC), HydRA turns off automatically and an error message is displayed.

Experimental parameters

The experiments are conducted at a fixed flow rate of approx. $1 \text{ cm}^3/\text{min}$ for both pumps (i.e., reservoir tanks) which amounts to a total volume flow rate through the rock sample of $2 \text{ cm}^3/\text{min}$. The temperature range is chosen according to the conditions at the natural injection wells and is set to 20, 60, and $150 \text{ }^\circ\text{C}$. The pressure is set to 20 bar (operational pressure), 300, and 350 bar (reservoir pressure).

The parameters recorded during the experiments are mass flow, temperature, upstream pressure, downstream pressure (resulting in differential pressure over the rock sample), and the confining pressure. In Table 1, the selected experiments and their respective conditions are listed.

Table 1 Experimental parameters of selected experiments

Experimental run	Temperature (°C)	Pressure (bar)	Barite concentration (mg/L)	Flow rate (cm ³ /min)	Duration of the experiments (h)	Sample name
PV10	20	20	112.3	2	24	12.1
PV09	20	300	111.0	2	24	8.2
PV07	60	20	216.7	2	~ 14	7.2
PV14	60	300	219.0	2	~ 18	17.1
PV06	60	350	219.0	2	~ 19	7.1
PV13	150	300	358.0	2	~ 11	16.1

Rock sample

This study focuses on porous media and thus the experiments are conducted with rocks of the Buntsandstein Group, which is, inter alia, one reservoir rock of the Bruchsal location (Herzberger et al. 2010). The rock samples, used for the experiments, belong to the Middle Buntsandstein that consists of the Eck-formation Horizon, the Bausandstein-formation, and the general conglomerate (Geyer and Gwinner 2011).

The rock was collected from a quarry close to Lahr in the Black Forest, at the eastern border of the Upper Rhine Graben. Blocks of around 300–400 mm length and width and a height of 150 mm were cut out. In the laboratory, the cores were brought to the correct dimensions of 25.4 mm in diameter and 50.8 mm in length.

Fluid-numerical modeling

In order to model the solution, which was used for the percolating of the rock sample, the software PHREEQC (Parkhurst and Appelo 2013) is used. In a first step, the salt concentration of the solution (NaCl, CaCl₂) was calculated. In the second step, these values were used as input parameters to model the required barite and sulfate concentrations with a saturation index (SI) of 1.75 according to

$$SI = \log \frac{IAP}{LP}, \quad (1)$$

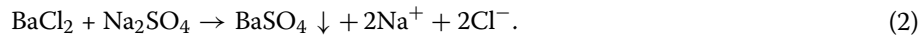
where IAP is the ion activity product and LP the solubility product (Tutolo et al. 2015; Merkel and Planer-Friedrich 2008).

The calculations were made using the geochemical software PHREEQC Version 3 and the Ilnl database (Parkhurst and Appelo 2013).

Fluid composition

An artificial fluid that reproduces the major hydrochemistry of Soultz-sous-Forêts was prepared according to the geothermal fluid composition described in Sanjuan et al. (2010). The pH value of the solution is in the range of 5.3–5.5. This geothermal fluid contains Na⁺, Ca²⁺, and Cl⁻ and therefore the artificial fluid was prepared using the salts NaCl and CaCl₂ * H₂O. To gain the desired concentrations for Na⁺ (1.27 mol/L) and Ca²⁺ (0.17 mol/L), 74.4 g/L NaCl and 25.3 g/L CaCl₂ * H₂O were used. The resulting concentration of Cl⁻ is 1.62 mol/L.

During an experiment, one reservoir tank contains the artificial fluid (consisting of NaCl and CaCl₂) together with a modeled concentration of BaCl₂, while the other reservoir tank is filled with a similar artificial fluid (NaCl and CaCl₂) and a modeled concentration of Na₂SO₄. At the inlet of the rock sample (Fig. 1), the two fluids are mixed and the resulting solution shows a well-defined supersaturation with respect to barite [see formula (2)]



Hydraulic parameters

Permeability

To monitor the permeability changes during the experiment and to control the values of the permeability before and after the experiment, the differential pressure was determined by measuring the fluid pressures up- and downstream of the sample. The differential pressure was adjusted, depending on the flow rate used. These descriptive values were taken before and after the percolation experiment. By using Darcy's law, the calculation is as follows:

$$k(t) = \frac{\eta Q l}{A \Delta p(t)} \quad (3)$$

$k(t)$ is intrinsic permeability (m²) ($1\text{D} = 9.87 \times 10^{-13}\text{m}^2$); η is dynamic viscosity of the fluid [Pa s]; l is length of the sample (m); Q is flow rate (m³/s); A is cross section (m²); and Δp is differential pressure [Pa] (1 bar = 100 kPa).

The permeability measurements were conducted with the HydRA facility by using distilled water with a well-known viscosity. Further known parameters are the dimensions of the sample and the differential pressure, which was recorded by the pressure load cells (Fig. 1). So the requirements for a standardized permeability calculation according to DIN 18130-1 (1998) are fulfilled for each experiment and thus the complete saturation of the sample with distilled water and the measurement should be performed in the range of linear flow to ensure a Darcy flow (Soni et al. 1978).

Effective porosity

To gain more information on the inherent properties of HydRA and to characterize the flow-through behavior of the mounted rock sample, tracer tests using different salt solutions were carried out. With K and Li as tracer cations, it is possible to determine the effective porosity of the rock samples according to

$$n_{\text{eff}} = \left(\frac{Q * t_{0,5}}{V} \right), \quad (4)$$

where Q is the flow volume (cm³/min); V is the volume of the sample (cm³); $t_{0,5}$ time to breakthrough (min) (Klotz et al. 1982).

The composition of the tracer solution is the same as for the background electrolyte solution described above, with the inert tracer being added.

By measuring the initial porosity of some samples, before and after the experiments, it was noted that the changes of the porosity values were in the range of measurement accuracy.

Analytical methods

Rock–mineralogical analysis

Scanning electron microscopy (SEM)

Scanning electron microscopy was used to analyze the mineralogy of the sandstone rock samples before and after the experiment. Thin sections were prepared as longitudinal sections of this cylindrical rock samples with a thickness of 30 μm at the Mineralogical and Geochemical Lab, Institute of Applied Geoscience (AGW), KIT.

The thin sections were sputtered with an 8-mm-thick layer of Au/Pd (80/20), prior to the analysis, using a Cressington Sputter Coater 208. SEM analyses were performed with a LEO Gemini 982 from Zeiss. The determination of the chemical composition of micro areas, including line scans, was performed using an Oxford INCA Penta FETx3 EDX-System. Both instruments are housed at the IKFT (Institute of Catalysis Research and Technology) at KIT. One image of the initial mineralogical composition was made at the KIT-LEM (Laboratory of Electron Microscopy), where the sample was sputtered with a layer of carbon.

X-ray computer-assisted tomography (CT)

One CT analysis was performed for an unpercolated rock sample that was reworked to a diameter of 40 mm to fit into the core holder of the CT. Tomographic 3D-datasets were recorded with the CT scanner ProCon X-Ray. The measurements were performed at an acceleration voltage of 130 kV, a current of 180 μA , and an exposure time of 180 ms. The datasets were reconstructed with a Volex reconstruction engine (Fraunhofer-Allianz Vision 2012). The reconstruction algorithm is based on a Radon transform by convolution and back filter (Feldkamp et al. 1984). Corresponding voxel size is 21.87 μm . After the 3D volume reconstruction, the images were processed using the software package Avizo 9.1 (ZIB 2016).

X-ray fluorescence (XRF)

The initial chemical rock composition was analyzed by X-ray fluorescence. Analyses were performed with a wave length dispersive XRF (S4 Pioneer, Bruker AXS). For the analysis, the rock samples were crushed and grinded to powder. Afterwards a fusion bead was synthesized and the measurement was performed against a matrix-matched calibration at 60 °C and 300 bar.

Inductively coupled plasma mass spectrometry (ICP-MS)

The major and trace element geochemistry of the rock samples (7.2, 8.2, 15.1, and 16.1) before and after the experiment was determined by ICP-MS (X-series 2, Thermo Fisher Scientific) after HNO_3 –HF– HClO_4 acid digestions of the powdered material (100 mg). To assure a complete silicate decomposition, 40% HF (Suprapur), 70% HClO_4 (Normapur), and the pre-oxidized sample (65% HNO_3 , sub-boiled) were heated in a closed vessel for 16 h at 120 °C. After evaporating the acids to incipient dryness, the residue was re-dissolved in 65% HNO_3 and evaporated again (three times) for purification purposes. The final residue was dissolved in 50 mL of ultrapure water. To assure the quality of the whole procedure, three blanks and two certified reference materials [GS-N, SY-2; Govindaraju (1994)] were included into the digestion process (accuracy: $\pm 10\%$). The

reproducibility ($\pm 5\%$ for most elements) was checked by digesting one sample in triplicate. The quality assurance for the ICP-MS measurement was done by including the certified reference material CRM-TMDW-A (High-Purity standards, Inc.) into the protocol (accuracy: $\pm 7\%$ for most elements).

Fluid analysis

A total of 25 fluid samples was collected for each experiment at the sampling point (Fig. 1) and analyzed on their Ba concentration using inductively coupled plasma optical emission spectrometry (ICP-OES). Hereby, samples 1 and 2 are the starting solutions [background electrolyte with BaCl_2 (1) and with Na_2SO_4 (2)], while samples 3 and 4 were taken from the mixture of the solutions (background electrolyte with BaSO_4) to determine the real inlet concentration. To prevent further reactions of Ba^{2+} and SO_4^{2-} , the final solutions of the flow-through experiment had to be diluted immediately after sampling.

The sampling began 30 min after starting the pumps, since the effluent needs 30–35 min to reach the sampling station. Samples were taken after 30, 32, 36, 38, 40, 50, 60, 90, 160, 210, and 270 min (calculated from the start of the run). Each sample was collected manually with a 100 μL pipette and transferred into a bottle containing HNO_3 (0.3 mL, conc., sub-boiled) with the internal standard Yttrium and distilled water (9.6 mL) to gain the predefined dilution of 1:100. During the night, five samples were taken using an automatic sampling carousel and on the second day sampling was done every 60 min until the test duration of 24 h was over.

All samples were analyzed, processed, and evaluated with an ICP-OES Optima 4300 DV (PerkinElmer Instruments) and the implemented software. The calibration of the ICP-OES was performed with the background electrolyte. For the measurements, the solutions had to be diluted by a factor of 1:100. The used specific wave lengths were 455.403 and 493.408 nm with a detection limit of 1 $\mu\text{g Ba/L}$.

Results

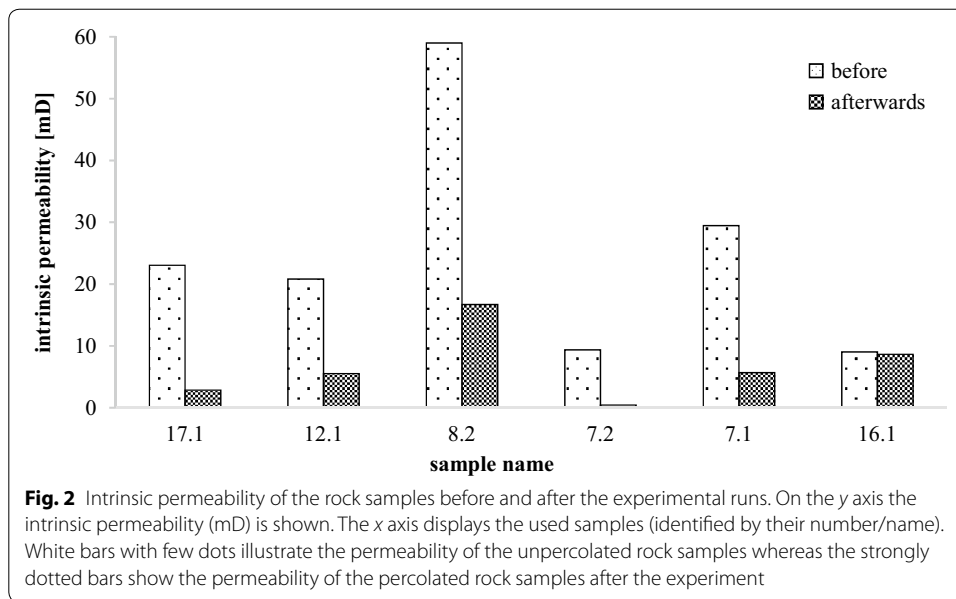
Hydraulic parameters

Permeability

To detect permeability changes during the experiments, two pressure cells (one upstream and one downstream of the rock sample) were used. Measurements were done with distilled water before and after the experimental runs. For a measurement, the rock sample was fully saturated with distilled water and then installed to the core holder before it was mounted into the autoclave. Then temperature and pressure were adjusted. During the measurement, it was necessary to adjust the stable laminar Darcian flow.

Figure 2 illustrates the intrinsic permeability of the rock samples of the analyzed experimental runs. For all rock samples, the permeability is higher before the flow-through experiment than afterward (Fig. 2).

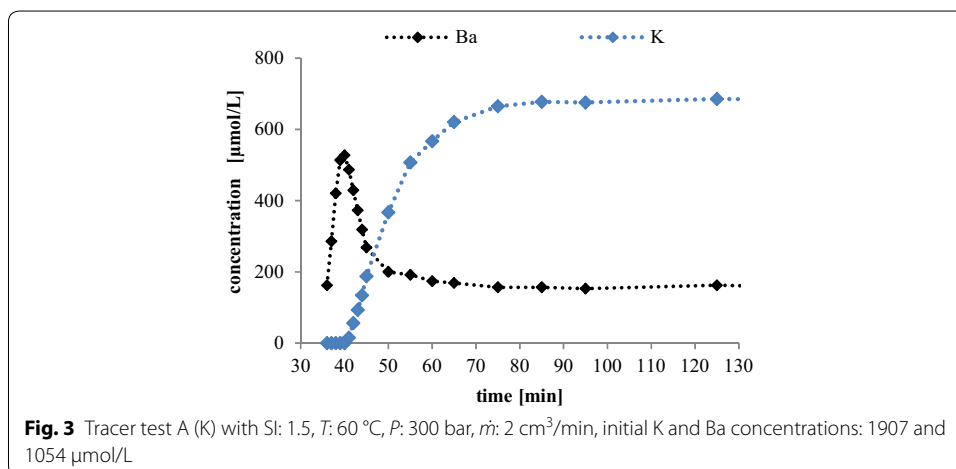
A considerable difference in the rock permeability can be found for sample 17.1 with an eightfold decrease from 23 to ~ 2.9 mD within 1100 min. For sample 12.1 only a 3.6-fold decrease is detectable with values of 20 mD before and ~ 5.5 mD after the experiment. With 59 mD the sample 8.2 has the highest initial permeability of all samples, which dropped to 17 mD after 24 h. Sample 7.2 is, apart from sample 16.1, the sandstone with

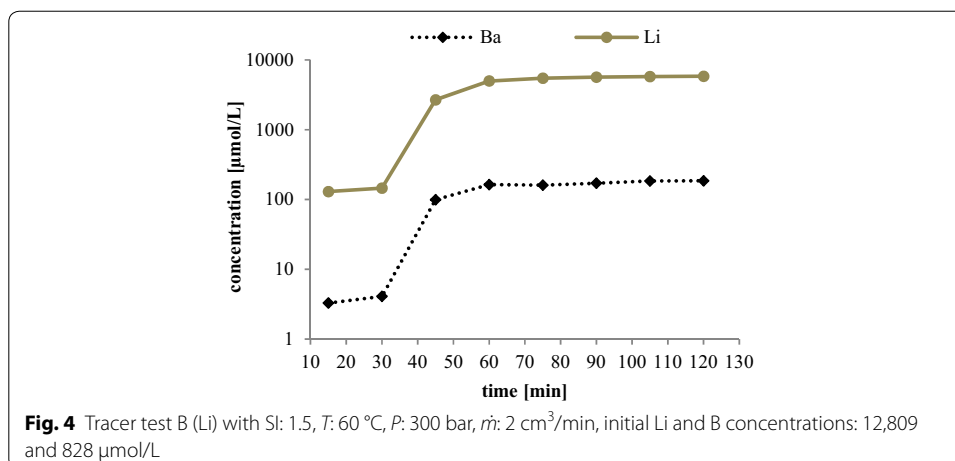


the lowest initial permeability of ~ 9 mD, which drops to 0.4 mD and thereby shows a ten-fold decrease. A fivefold decrease in permeability can be determined for sample 7.1 with a drop from 29.5 to 5.7 mD (duration of the run: 1155 min). Almost no permeability drop is observed for sample 16.1, which shows an initial permeability of 9 mD that declines to 8.6 mD. No particle clogging is observed at the inlet of the rock sample, while in some cases a minor amount of sand grains are observed between the sample and the tube.

Effective porosity

Tracer breakthrough Figures 3 and 4 show the Ba, Li, and K concentrations as evolution over the experiment duration in minutes. For the experiments, a barite saturation index (SI) of 1.5 is chosen. The temperature was set to 60 °C, the pressure was 300 bar, and the flow rate was adjusted to 2 cm³/min. For the two tracer tests (test A and test B), two different rock samples were used.





In test A (Fig. 3, 19 hydrochemical analyses) K was the tracer. The initial concentrations of K and Ba were 1907 and 1054 µmol/L, respectively. According to Fig. 3, the Ba concentration reaches a sharp maximum concentration of 528 µmol/L after 40 min before it approaches an almost stable concentration of 156 µmol/L. The increase in the K concentration starts after 41 min from 15 µmol/L to reach an almost stable value of 653 µmol/L after 65 min. The loss of K is ~ 65% (1907–653 µmol/L).

For test B (Fig. 4, seven hydrochemical analyses), the concentrations are plotted logarithmically to improve clarity. The initial concentrations of Li and Ba are 12,809 and 828 µmol/L, respectively. According to Fig. 4, Li is detected after 15 min with a concentration of 138 µmol/L. Later, the concentration increases to a value of approx. 2680 µmol/L before it reaches an almost stable value of 5688 µmol/L after 75 min. After a test duration of 15 min, Ba is detected with a concentration of 3 µmol/L. Within 30 min the concentration of Ba increases to a value of 99 µmol/L and after a test duration of 90 min an almost stable concentration 180 µmol/L is reached. The overall loss of Li is ~ 56% (12,809–5688 µmol/L).

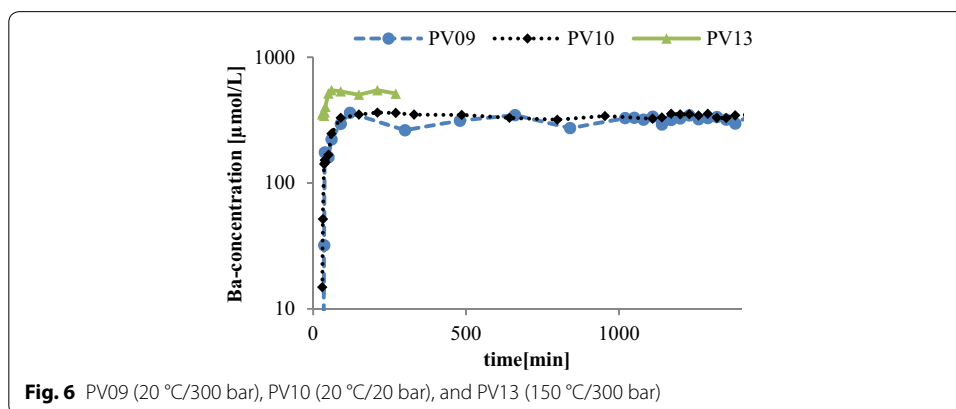
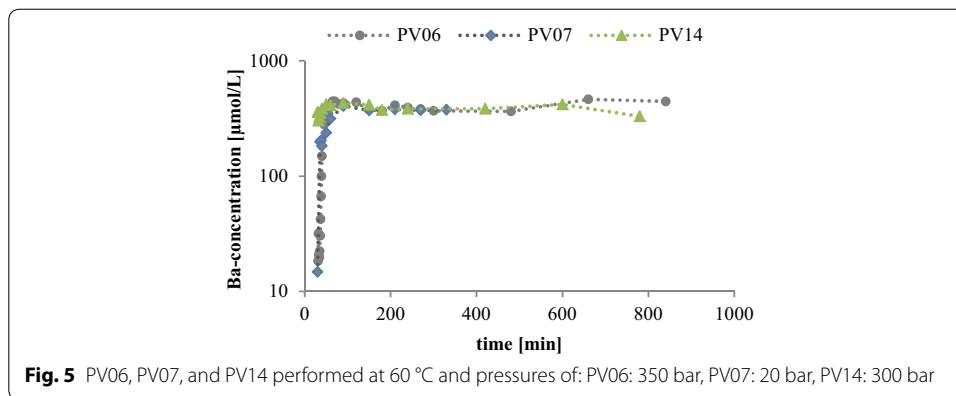
The effective porosity is calculated with the following input parameters: $Q = 2 \text{ cm}^3/\text{min}$, $t_{0.5}(\text{K}) = 365 \text{ min}$, $t_{0.5}(\text{Li}) = 127 \text{ min}$, and the volume for the samples is 25.54 cm³. For the Tracer test A (with K) the effective porosity of the rock sample n_{eff} is around 28.6, while for the second Tracer test B (with Li) n_{eff} is around 10.

Fluid–Ba concentration

In Table 1, selected experimental runs are listed with their sample names and the respective temperature, pressure, and flow conditions. For all experiments, the saturation index of barite was calculated with PHREEQC (Parkhurst and Appelo 2013) and had a value of 1.75.

Prior to an experiment, the pipes and the rock samples were percolated with distilled water. With the start of the experiment, the distilled water in the two reservoir tanks was replaced by the artificial fluid.

In Figs. 5 and 6, the dissolved Ba concentrations in µmol/L (logarithmic) are plotted over the duration of the experiment in minutes. All curves are characterized by an initial increase of the Ba concentration. This feature can be interpreted as a result of an initial



dilution by the residual distilled water in the sample before the whole system is flooded by the undiluted, Ba-containing artificial fluid. All Ba concentrations increase up to a maximum value and remain more or less constant afterward.

Figure 5 shows the Ba concentration curves for the experimental runs PV06 (60 °C/350 bar), PV07 (60 °C/20 bar), and PV14 (60 °C/300 bar). The initial Ba concentration for the three runs is 1487 $\mu\text{mol/L}$. The Ba concentration in PV07 shows a distinct peak of 406 $\mu\text{mol/L}$ after 90 min before it approaches an average concentration of 375 $\mu\text{mol/L}$, resulting in a total Ba concentration loss of approx. 75%. PV14 also shows a distinct peak in the Ba concentration after 90 min with a value of 431 $\mu\text{mol/L}$, before it decreases to an average concentration of 378 $\mu\text{mol/L}$ (total Ba concentration loss of approx. 74%). In PV06, the distinct peak with a Ba concentration of 445 $\mu\text{mol/L}$ is observed already after 70 min. Later the curve approaches an average concentration of 381 $\mu\text{mol/L}$ resulting in a total Ba concentration loss of approx. 74%.

Figure 6 illustrates the evolution of Ba concentrations for the experimental runs PV09 (20 °C/300 bar), PV10 (20 °C/20 bar), and PV13 (150 °C/300 bar) using a logarithmic scale. The initial Ba concentration in PV09 is 763 $\mu\text{mol/L}$. A distinct Ba peak with a maximum value of 361 $\mu\text{mol/L}$ is observed after 120 min. Later an average concentration of 315 $\mu\text{mol/L}$ is approached, implying a total Ba concentration loss of approx. 58%. PV10 (Fig. 6) has an initial Ba concentration of 775 $\mu\text{mol/L}$ and a distinct peak with a Ba concentration of 362 $\mu\text{mol/L}$ that develops after 210 min. Afterward, the Ba concentration

decreases to an almost stable value of 340 $\mu\text{mol/L}$, resulting in a total Ba concentration loss of approx. 56%. In PV13, the initial Ba concentration is 2613 $\mu\text{mol/L}$ which drops very fast to a value of approx. 360 $\mu\text{mol/L}$. Then the concentration increases up to a maximum value of 547 $\mu\text{mol/L}$ before it decreases again to 503 $\mu\text{mol/L}$ after 150 min. The final resilient concentration value of this experimental run is 547 $\mu\text{mol/L}$ Ba after a test duration of 210 min. The total concentration loss of Ba is approx. 78%.

Mineralogical composition

Initial rock

The used sandstone of the stratigraphic unit Bausandstein–Geröllsandstein (su–sm) contains high amounts of SiO_2 , while Al_2O_3 and K_2O are present in a low percentage range, mainly resulting from minor feldspar content (Table 2). The values of all other major elements are very low. In addition, the chemical composition of the sandstone given by Hirsch (2008) is given as a reference. A comparison of the values shows that the composition of the sandstone has a poor variance. Therefore the rock samples can be considered as representative for the stratigraphic unit.

The sandstone is red colored and medium-grained. It is quartz-rich with a clay matrix. The quartz and K-feldspar grains are rounded to subrounded (Fig. 7). Locally, clay enrichments (called Tongallen) are observed but test pieces with these textures were avoided as also pieces with prominent layering. Some clay minerals are found as space filling (Fig. 8). The mica content of less than 1 vol % is very low, the content of hematite/Fe-hydroxide is ≤ 1 vol % and the modal content of matrix reaches values of up to 5 vol %.

Table 2 Major element composition of the initial sandstone compared to the reference values of Hirsch (2008)

Mass %	SiO_2	Al_2O_3	K_2O	TiO_2	Fe_2O_3	Na_2O	MgO	CaO
IAM-AWP (2016) ^a	93.70	3.55	2.26	0.33	0.28	0.10	0.07	0.07
Hirsch (2008)	94.54	2.89	1.93	0.03	0.25	0.09	0.04	0.06

^a Performed at 60 °C and 300 bar (IAM-AWP—Institute for Applied Materials, 2016)

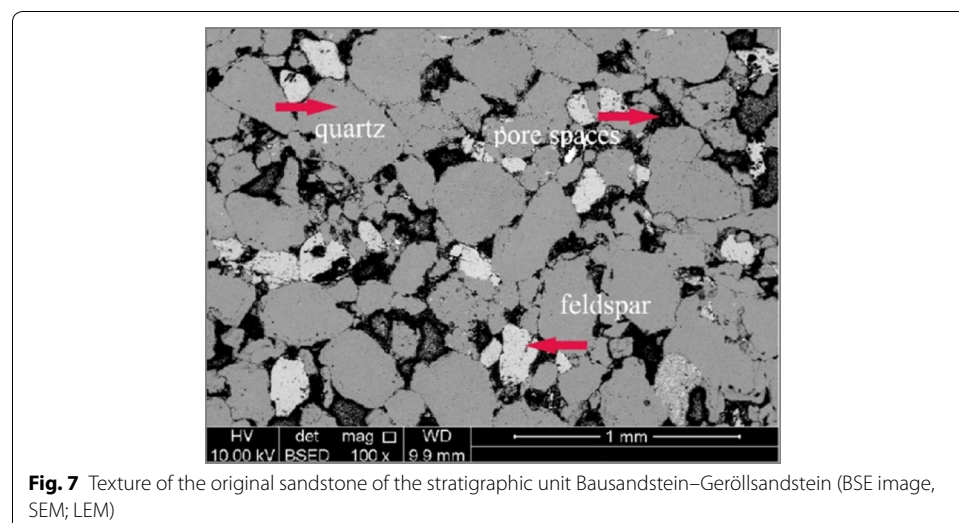
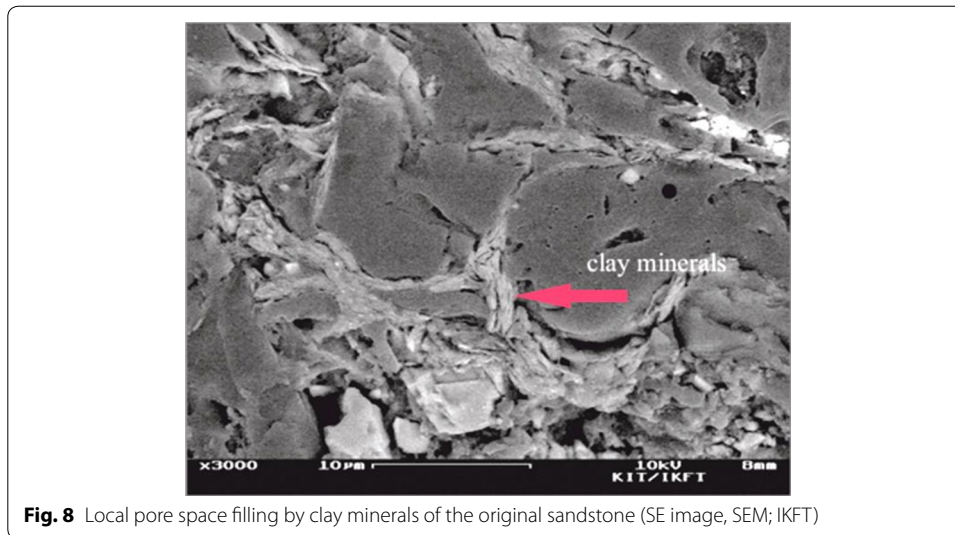
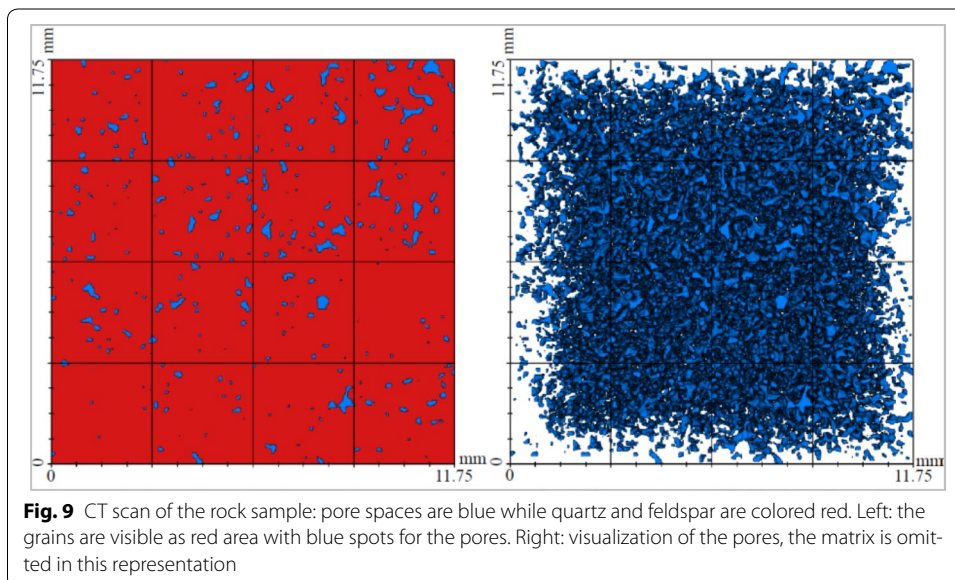


Fig. 7 Texture of the original sandstone of the stratigraphic unit Bausandstein–Geröllsandstein (BSE image, SEM; LEM)



Similar results can also be found by CT scans (Fig. 9). The images are segmented into binary images of pores (blue) and grains (red) by applying a watershed algorithm on the unfiltered gray value images (Beucher and Lantuéjoul 1979). Following this procedure, the pore space of the reference sample is 5.6 vol % and the amount of quartz and feldspar is calculated to approx. 94 vol %.

Hirsch (2008), among others, analyzed the same rock during an investigation of the different sandstones used to build up the Freiburger Münster. For this purpose she examined the rocks regarding their mineralogical composition, density, porosity, water absorption coefficient, and the origin of the sandstone. She examined similar mineralogical and geochemical compositions as well as values for porosity like those observed in the samples of this study.



Flow-through rock

In situ precipitations of barite crystals Barite precipitations are provoked by using a barite-supersaturated solution. After several pre-experiments, the barite crystallization was successfully provoked in the pore spaces of the sandstones and not in the pipe or at the inlet area. The barite crystals are visible as white crystals in BSE images of the SEM (Figs. 10, 11, 12, 13, 14, 15, 16). Supersaturation of more than 1.75 led to precipitations of barite in the pipes and at the inlet of the sample while supersaturation from 1 to 1.75 led to poor amounts of barite precipitation, which were not detected by the analytical methods used. Hence a supersaturation of 1.75 was chosen and worked reliably in all experiments.

Detailed investigation with SEM shows that barite occurs in only some of the pore spaces of an individual rock samples, whereas others remain almost unchanged. The growth features observed for barite imply a crystallization sequence in the experiments.

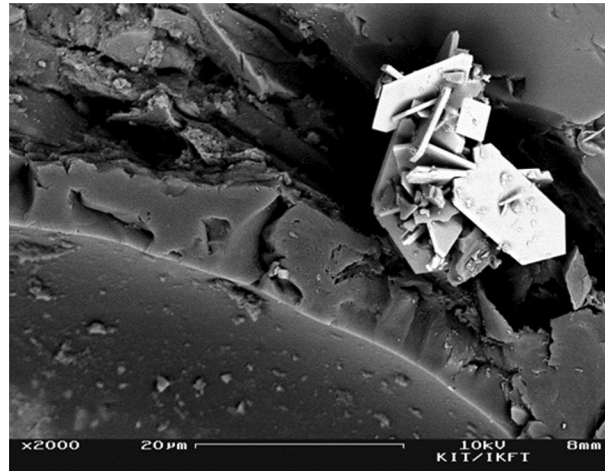


Fig. 10 Growth of euhedral, tabular barite crystals sample 12.1 (PV10; 20 °C/20 bar)

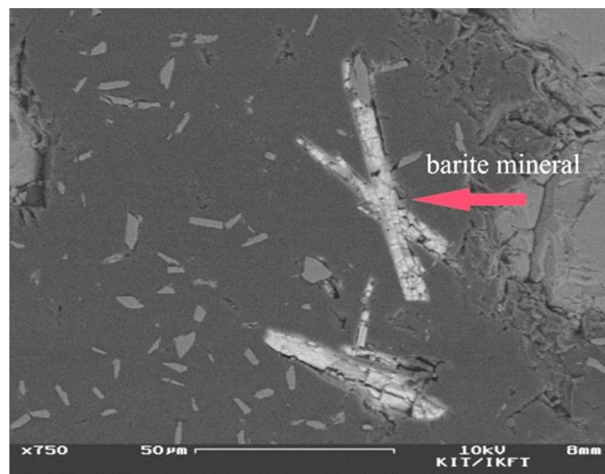


Fig. 11 Intergrowth of barite, sample 7.2 (PV07; 60 °C/20 bar)

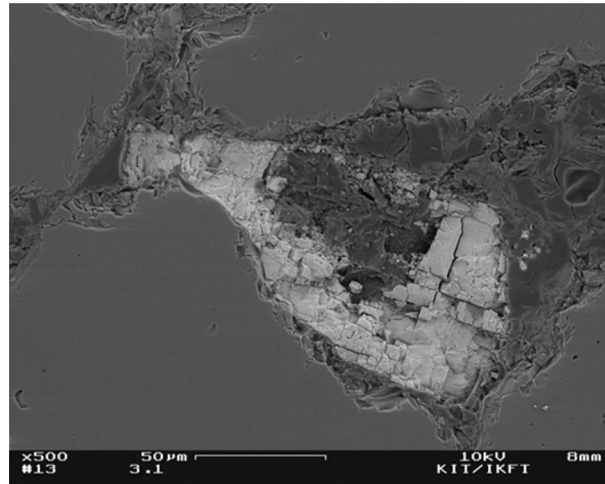


Fig. 12 overgrowth of illite by barite sample 3.1

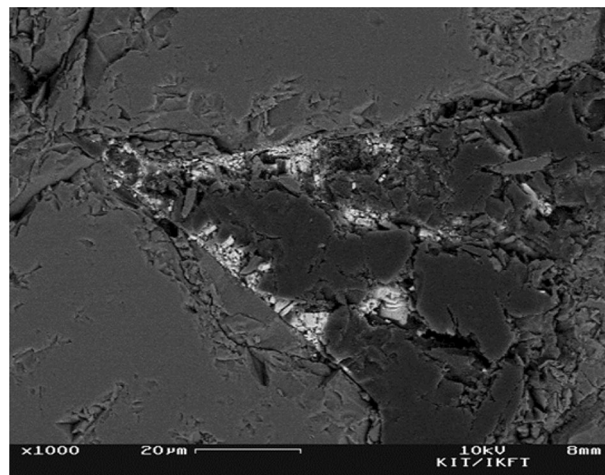


Fig. 13 Preferential accumulation of the barite crystals in the tips of the pore spaces, sample 14.2 (180 °C/350 bar, the experiment is not part of this study, since HyDRA stopped the experiment automatically after 9 h)

In the beginning, the growth of the barite crystals is tabular (Fig. 10) with a size of approx. 15 μm in the larger pore spaces. Once a barite crystal is formed, it acts as a seed and is overgrown by further barite precipitations forming a crystal agglomerate (Fig. 11). The crystal shape of the agglomerate is mostly platy with a well-defined cleavage. Crystal agglomerates can be found in a part of the pore spaces of all sandstone samples after experiment, which were either unfilled before the experiment or partially filled with clay minerals and hematite. In the latter case, the barite overgrows the illite along the margins of the pore (Fig. 12). Quartz grains have smooth surfaces with small holes and often show dissolution edges (Fig. 18), whereas such features are absent in the feldspar. Especially in the smaller pores and cracks, subhedral barite crystals grow together forming crystal aggregates. With increasing growth or narrowing of the pore spaces, the crystals

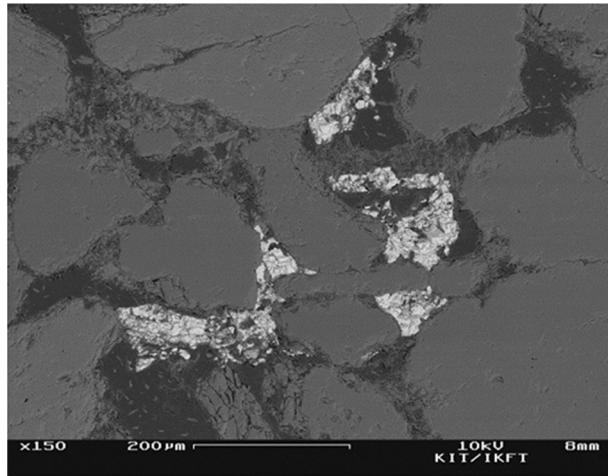


Fig. 14 Growth of barite crystals in some of the pore spaces, sample 7.2 (PV07; 60 °C/20 bar)

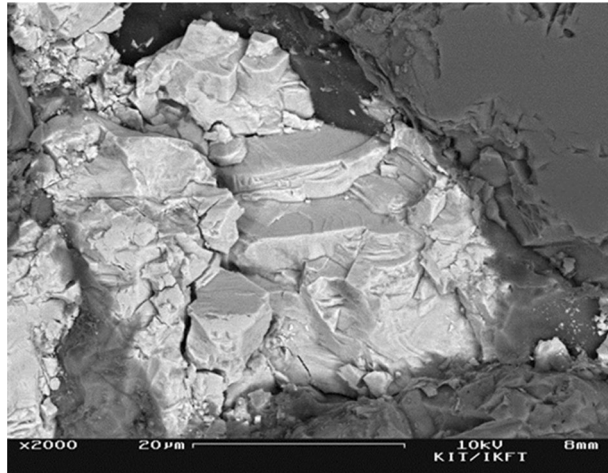


Fig. 15 Crystal agglomeration of barite, sample 7.2 (PV07; 60 °C/20 bar)

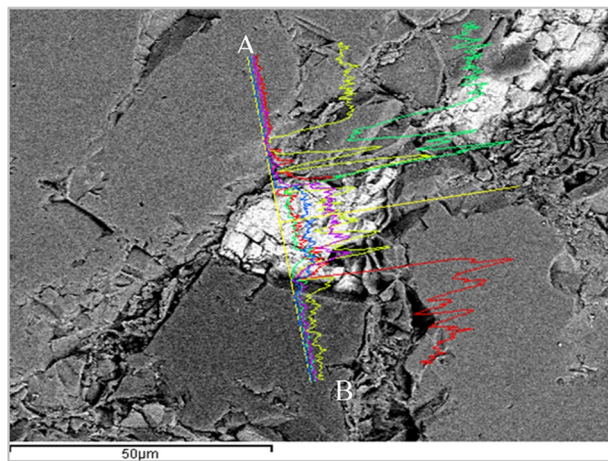


Fig. 16 Position and results (for details see Fig. 17) of a line scan over a barite crystal to analyze its chemical composition

preferentially accumulate at the bottlenecks of the pore spaces (Fig. 13). This can lead to a clogging of the whole interspaces. Finally, the pore spaces and cracks get completely filled with barite crystals (Figs. 14 and 15).

Most of the crystals are weakly fractured. This fragmentation is probably caused by the permeability measurement after the experimental runs and the subsequent sample preparation steps, i.e., sawing and preparation of the thin sections.

The line scan (Figs. 16 and 17) shows the intensities of the characteristic x-ray signals of Si ($K\alpha$), O ($K\alpha$), C ($K\alpha$), S ($K\alpha$), and Ba ($L\alpha$) over the distance from the starting point of the scan.

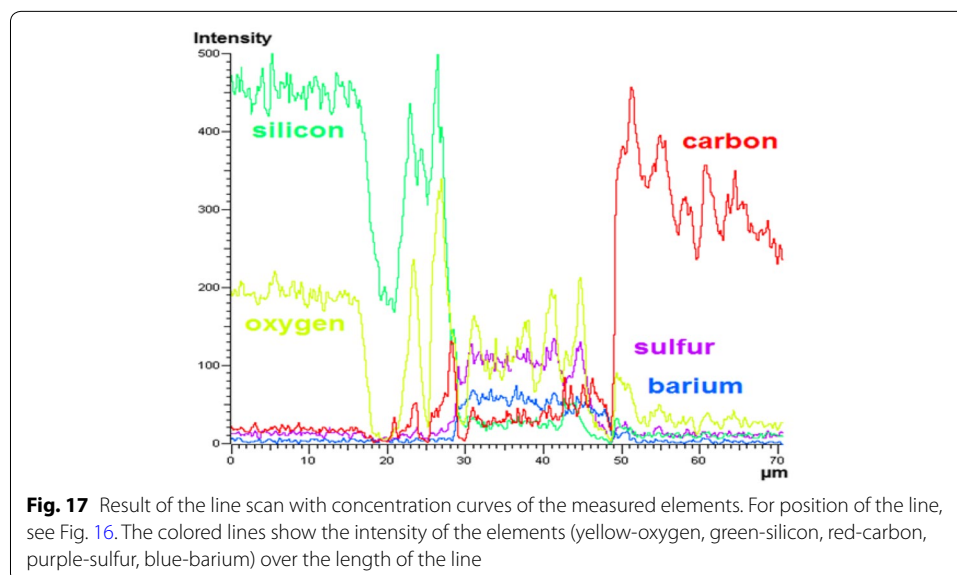
Precipitations of secondary mineral phases During investigation with SEM, some spherical structures were observed, that only occur in some of the reacted samples (Figs. 18 and 19) as small spheres with diameters of $< 1 \mu\text{m}$. They grew on the surfaces of sandstone minerals, also including the newly formed barite in the pore spaces. Accordingly, the appearance of these phases is not related to replacement of a special mineral phase, or a specific experimental condition.

Energy dispersive XRF measurements with the SEM reveal that these phases consist of O (53.27 wt %), Si (30.12 wt %), and C (15.57 wt %). The residue to 100% can be attributed to the sputtering materials Au and Pd.

Trace elements

The geochemistry of the rock samples was further analyzed with regard to trace element composition after full acid digestion. The geochemistry of the sandstone was characterized before and after the experiments and thus allows the investigation of chemical changes during the experiments due to water–rock interaction processes.

After the experiments, the samples 7.2, 8.2, 15.1, and 16.1 (see Table 1 for experimental conditions) show a decrease in the concentrations of Al, K, Na, Ti, Rb, Sn, and Tl, when compared to the corresponding initial samples. Apart from Na, these elements



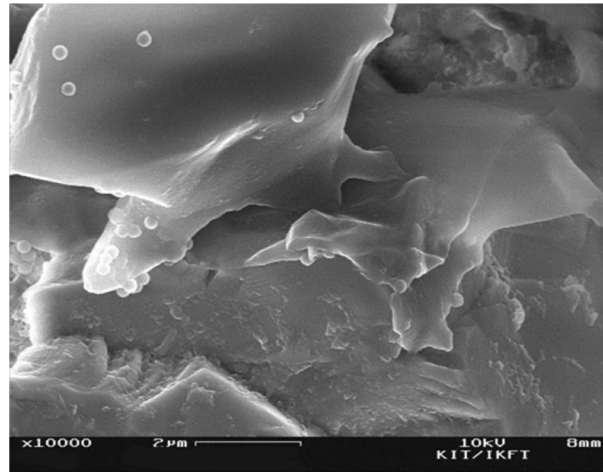


Fig. 18 SEM (SE image) of barite covered with spherical phases, sample 10.1 (20 °C/200 bar)

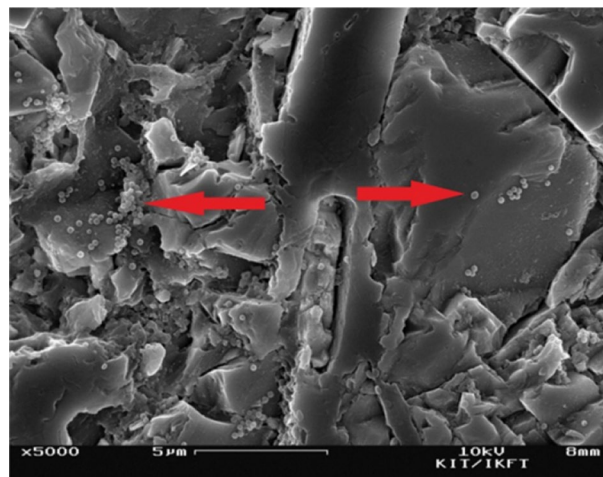
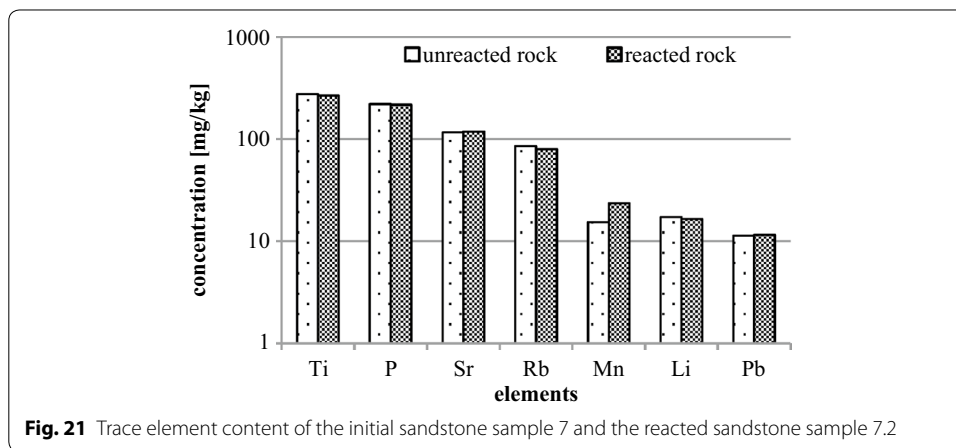
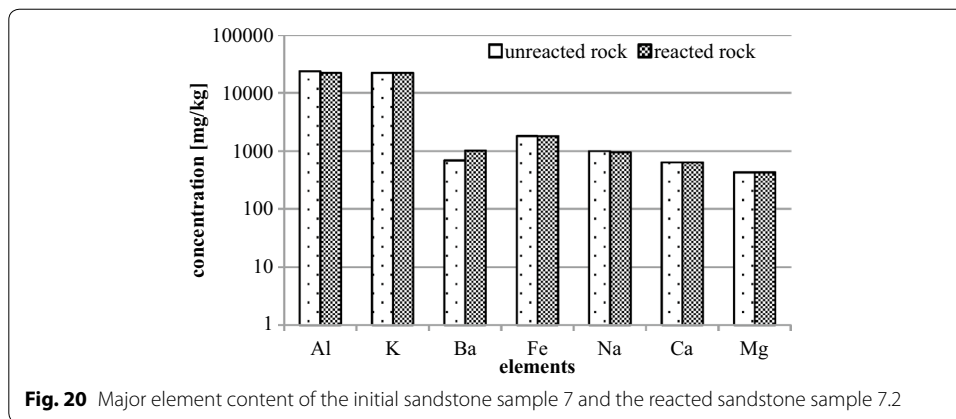


Fig. 19 SEM (SE image) of barite with numerous spherical phases formed on its crystal phases, sample 7.2 (PV07; 60 °C/20 bar)

were not present in the initial artificial fluid, but they were found in the fluid after percolating the sandstone. Consequently, they were released from the sandstone due to fluid–rock interactions. In all rock samples, higher Ni and Ba concentrations can be detected after the experiments. The additional Ni likely originates from dissolution and transport of the pipe material to the sandstone, while the increase in the Ba content is due to the barite precipitation.

In Figs. 20 and 21 the results of the analyses of the rock samples 7 and 7.2 are compared.

Decreasing concentrations are observed for the elements Fe, Ca, P, Li, Cr, Co, Cs, Cu, U, Sb, and Mo. The most significant decreases were detected for Cr (5.39–4.12 mg/kg, decrease of approx. 23%), Co (1.36–0.43 mg/kg, approx. 68%), Cs (3.33–2.53 mg/kg, 24%), and Mo (0.10–0.07 mg/kg, 32%).



Increasing concentrations are measured for Ba, Mg, Sr, Mn, Pb, Y, V, Zn, Ni, As, and Cd with most significant increases for Ba (692–1024 mg/kg, approx. 32%), Mn (15.45–23.6 mg/kg, approx. 34%), Zn (3.61 up to 7.23 mg/kg, 50%), and Ni (2.95–46.5 mg/kg, approx. 94%).

Since the initial and reacted sandstone samples for geochemical analysis were taken from different regions of the cylindrical sample, differences in the composition are possible that this is not related to the experimental procedure and originate from natural heterogeneities (Additional file 1).

Discussion

Effect of temperature

Fresh test solution is supplied with a constant flow rate during the complete experiment duration. Therefore the reaction time remains the same resulting in a constant concentration and thus a constant precipitation of barite. According to the experimental results, the final Ba concentration in the fluid strongly depends on the temperature while pressure changes seem to be of minor importance. Ba losses of 56–63%, 74–75%, and 78% were found at temperatures of 20, 60, and 150 °C, respectively, indicating progressive Ba precipitation in the porous sandstone with increasing temperature.

However, it has to be taken into account, to get an SI of barite of 1.75, the input concentration of the NaSO_4 and BaCl_2 is much higher at 150 °C compared to the runs at 20 and 60 °C. This is reasoned by the solubility of BaSO_4 because this undergoes a maximum close to 150 °C (Blount 1977).

Some elements like K, Na, Rb, Al, P, or Sr show a higher concentration decrease in low temperature experiments (20 °C) compared to higher temperatures (60, 150 °C) indicating an increased dissolution of primary sandstone minerals at lower temperatures. This does not go in line with the known low solubility and general solubility with increasing temperature for most minerals like K-feldspar, mica, clay minerals, or apatite, that are present in sandstone. Rather it can be expected that dissolution and re-precipitation are dominant processes in the high-tempered experiments compared to washout effects of pre-experimental weathering at low temperatures. This fact is shown by Schmidt et al. (2017). He observed dissolution of quartz, illite, kaolinite, and feldspar and precipitation of analcime, chlorite, and albite at high temperatures (200 and 260 °C, experiment duration 45–55 days).

The elements Mn, P, Cr, Ni, Mo, and Ti, which show a concentration increase in the sandstones after the experiments, might originate from the pipe material of the apparatus.

Change of hydraulic parameters

Effective porosity In the tracer tests, more than half of the input quantity of the used tracer cations K and Li was lost during the percolation of the rock sample (Li: 65%, K: 58%). The shape of the K concentration curves, which was assumed to show a conservative behavior (Fig. 3), leads to the assumption that K accumulates in the rock sample through adsorption on negatively charged surface sites of clay minerals or Fe oxyhydroxides, while Ba passes the sample more or less unreacted. Thus a high peak can be observed at the beginning of the Ba concentration curve that rapidly decreases afterwards. In the test with Li (Fig. 4), the Ba concentration behaves completely different. In this experiment, the concentration curves of Ba and Li have the same shape and proceed almost parallel. Both curves increase until they reach an almost stable concentration after approx. 60 min.

The results of both tracer tests lead to the assumption that the used tracer cations K and Li are not suitable for the determination of the effective porosity of the present rock sample. The ions do not behave conservatively and therefore the calculations using formula (4) produce inaccurate results. The calculated porosity value for the test with Li is 10, while it is 28.6 for the test with K. This large difference in the porosity values is a further hint on the infeasibility.

Permeability changes All experimental runs show a decrease of the permeability of the reacted sandstones (Fig. 2) that is in accordance with the observed Ba precipitation using SEM analysis. The experimental runs at a temperature of 20 °C show a decrease of the permeability of approx. 68% for PV09 and approx. 75% for PV10. At a temperature of 60 °C the experimental runs PV 07, PV14, and PV 06 show higher decreases of 95, 90, and 80%, respectively. But in test PV13 at the highest used temperature investigated (150 °C), the decrease of the permeability is only 6%. This contradictory effect—lowest perme-

ability at highest temperature with largest loss in Ba concentration—may be due to the solubility maximum of barite around 150 °C.

The determination of the barite-precipitation mass was not feasible, because during the removal of the sample (out of the silicon tube) some rock material got lost and falsified the values. Additionally, the mass of the precipitated barite was extremely low and it was not possible to quantify it exactly. Therefore the relation between the permeability loss and the mass increase of barite cannot be given here.

Reaction sequence

Formation of barite

Due to the constant supply of barite-supersaturated solution, barite can grow continuously once precipitated, eventually until the pore spaces are completely filled. Barite is found as a part of the pore spaces of all the sandstone samples after the experiment. Smaller pores and cracks are completely filled with barite after experiments, whereas larger pores preserve open spaces. In larger pores, homogeneous nucleation and growth of barite is observed initially. As a result, large, subhedral to euhedral barite plates were formed in the beginning, which apparently grew inside the pores, away from a mineral surface. Subsequently grown barite preferentially overgrows already existing barite grains, indicating a change of the nucleation style from homogeneous to heterogeneous, i.e., on pre-existing crystal faces. In the smaller pores, heterogeneous nucleation and growth dominate. In this case, already the initial nucleation of barite preferentially occurs on the mineral faces surrounding the pores and these primary barite grains are then overgrown by the continuously precipitating barite during the experiment. Nucleation and growth mainly occurs in the tips of the pores and small cracks, finally leading to clogging of the open spaces. As a result the permeability of the sandstone decreases in most experiments.

Formation of secondary mineral phases

The observed microspheres are no residues of the abrasive, which was used to produce the thin sections. They are always well rounded and smaller than 1 µm in diameter; larger spheres are not found. Their morphology and O–Si–C-rich composition resembles that of polycarbosilane phases (Chen et al. 2011). Their small grain size and their formation on the crystal faces of the sandstone phases, also including the newly formed barite suggest that they form late, possibly during cooling of the sample. Their occurrence implies elevated Si concentrations of the solution after reaction and may be related to the observed dissolution of quartz during the experiment (Fig. 18).

Implications for geothermal operation

The most relevant information for geothermal energy usage that can be concluded from the experimental runs of this study is the drastic change of the permeability in the reservoir rock. This observation is definitely decisive for the profitability of a geothermal power plant. If the permeability of the reservoir rock is high, high flow rates can be expected. At the discharge wells, which are considered in this study, the capacity of the reservoir rocks is of major relevance for the return of the used geothermal fluid to the underground. If the permeability is decreasing with time, further investments for

cost-intensive compensation measures like active pumping (to press the fluid back into the underground) and/or chemical enhancing methods might become necessary.

Conclusions

In the present work, HydRA, an apparatus for performing experiments under geothermally relevant conditions, was developed, built, and put into operation. Using the HydRA facility it was also possible to fulfill the second aim of this work, the experimental investigation of the effects of barite precipitation in reservoir rocks under similar temperature and pressure conditions like those observed in the Upper Rhine Graben.

For this purpose also a method for inducing barite precipitation in the rock sample during percolation of a barite-supersaturated solution was developed and tested. The method, in which two solutions with different compositions are mixed at the entry of the sample, offers the opportunity of studying the influence of in situ precipitation during forced flow-through.

The experimental part of this study focused on possible changes of the permeability of reservoir rocks. A strong decrease of the permeability of the present reservoir rocks due to barite precipitation was observed in most experimental runs and different stages of pore clogging due to the barite precipitation were identified in the samples and visualized via SEM. This is of special importance for the operators of geothermal power plants, since the permeability of reservoir rocks is decisive for the profitability of a geothermal power plant. If the permeability at a geothermal site decreases, cost-intensive compensation measures have to be initiated.

Additionally, mineral dissolution in the sandstone was observed as a result of water–rock interaction during flow-through even in the short experimental residence times. In geothermal power plants, the temperature and pressure reduced fluids (by that the saturation degree of some mineral phases are raised up) would be injected into the reservoir rocks where they could alter the composition of the reservoir rocks drastically.

In forthcoming experiments, the residence time of the fluid in the sample should be elongated. This can be realized by reducing the flow rate. In the future, the HydRA facility can also be used to investigate other rock compositions, according to existing geothermal reservoirs. Moreover, the experimental setup can be adapted to simulate other geochemically relevant scenarios, as for example, a calcite supersaturation of the fluid. Even natural geothermal water can be used for the experiments. So HydRA offers many opportunities for performing experiments under geothermally relevant conditions.

Additional file

Additional file 1. Analyzed elements of the samples 7, 8, 15 and 16 before (unreacted) and after (reacted) the experimental runs.

Authors' contributions

PO performed the experiments and was the leader of the working group concerning HydRA. DK has contributed the financial support and the general idea how to realize such a flow-through apparatus. EE conducted the analyzing of the rock samples regarding the trace elements. She gave technical and analytical support to measure as good as possible the rock samples and contributed text. MZ performed all SEM and SEM–EDX measurements and contributed some text blocks. KD had read the manuscript several times and has given some constructive criticism. TK gave the initial idea to do this kind of research. All authors read and approved the final manuscript.

Author details

¹ Institute of Nuclear and Energy Technology, Karlsruhe Institute of Technology, Herrmann-von Helmholtz-Platz 1, 76344 Eggenstein-Leopoldshafen, Germany. ² RBS wave GmbH, Postfach 31 1508, 70475 Stuttgart, Germany. ³ Institute of Applied Geoscience-Division of Mineralogy and Petrology, Karlsruhe Institute of Technology, Kaiserstrasse 12, 76131 Karlsruhe, Germany. ⁴ Institute of Applied Geoscience-Division Geothermics, Karlsruhe Institute of Technology, Kaiserstrasse 12, 76131 Karlsruhe, Germany. ⁵ Institute of Catalysis Research and Technology, Karlsruhe Institute of Technology, Herrmann-von Helmholtz-Platz 1, 76344 Eggenstein-Leopoldshafen, Germany. ⁶ Institute of Applied Geoscience-Aquatic Geochemistry Division, Karlsruhe Institute of Technology, Kaiserstrasse 12, 76131 Karlsruhe, Germany.

Acknowledgements

We wish to thank David Hillesheimer and Michael Scholz for technical input and thoughts. A heartfelt thank you goes to Dominik Mayer and Klaus Thomauske for their technical support regarding HydRA. I would also point out the very conscientious work and great support of Sabine Baur. She gave me enormous assistance in the chemical laboratory and had always time for fruitful discussions. I am grateful to Sarah Herfurth and Andreas Friedrich, for reading the manuscript precisely.

For producing the thin sections, special thanks goes to Kristian Nikoloski from the Institute of Applied Geosciences (AGW). Additional ICP-MS analyses were performed at this Institute (Division of Aquatic Geochemistry), KIT, special thanks for that big support.

For the supply regarding the sandstone material, we thank Dr. Steffen Klumbach from the University of Bayreuth. To Mathias Nehler from the International Geothermal Centre of Bochum goes best wishes for contributing the CT scan of the reference rock. A big thank you goes to the Institute for Applied Materials, Department for Applied Materials Physics at the KIT for performing the XRF and the fluid analysis for this research.

Competing interests

The authors declare that they have no competing interests.

Availability of data and materials

All relevant data and material are presented in the main paper.

Consent for publication

Not applicable.

Ethics approval and consent to participate

Not applicable.

Publisher's Note

Springer Nature remains neutral with regard to jurisdictional claims in published maps and institutional affiliations.

Received: 4 May 2017 Accepted: 6 October 2017

Published online: 13 October 2017

References

- Banks J, Regensburg S, Milsch H. Experimental method for determining mixed-phase precipitation kinetics from synthetic geothermal brine. *Appl Geochem*. 2014;47:74–84.
- Beucher S, Lantuéjoul C. Use of watersheds in contour detection. Fontainebleau: Centre de Geostatique et de Morphologie Mathématique; 1979.
- Blount CW. Barite solubilities and thermodynamic quantities up to 300 °C and 1400 bars. *Am Miner*. 1977;62:942–57.
- Canic T, Baur S, Bergfeldt T, Kuhn D. Influences on the barite precipitation from geothermal brines. In: *Proceedings World Geothermal Congress 2015, Australia, Melbourne, 19–25 April 2015*. 2015.
- Chen Y, Li S, Luo Y, Xu C. Fabrication of polycarbosilane and silicon oxycarbide microspheres with hierarchical morphology. *Solid State Sci*. 2011;13:1664–7.
- Christy AG, Putnis A. The kinetics of barite dissolution and precipitation in water and sodium chloride brines at 44–85 °C. *Geochim Cosmochim Acta*. 1993;57:2161–8.
- Daubner M, Krieger V. Betriebsmessdatenvisualisierung und -erfassung mit OPAL (OPC-Panel Livegraph), KIT Scientific Reports 7558, Karlsruhe. 2010.
- DIN 18130-1. 05 Bestimmung des Wasserdurchlässigkeitswertes Teil 1 Laborversuche, Berlin. 1998.
- DIN EN 10088-3. Stainless steels—part 3: technical delivery conditions for semi-finished products, bars, rods, wire, sections and bright products of corrosion resisting steels for general purposes. Berlin. 2014.
- Feldkamp LA, Davis LC, Kress JW. Practical cone-beam algorithm. *J Opt Soc Am*. 1984;1(6):612–61. doi:10.1364/JOSAA.1.000612.
- Fraunhofer-Allianz Vision. Volex. Volume explorer software. Version 6.3., Fürth. 2012.
- Genter A, Evans K, Cuenot N, Fritsch D, Sanjuan B. Contribution of the exploration of deep crystalline fractured reservoir of Soultz to the knowledge of enhanced geothermal systems (EGS). *C R Geosci*. 2010;342:502–16.
- Geyer FO, Gwinner MP, Geyer M, Nitsch E, Simon T. *Geologie von Baden-Württemberg*, 5. Auflage, 627 Seiten, 185 Abbildungen, 4 Tabellen. ISBN: 978-3-510-65267-9. Schweizerbart. 2011.
- Govindaraju K. Compilation of working values and sample description for 383 geostandards. *Geostand News*. 1994;18:1–158.

- Herfurth S, Orywall P. Annual report 2015 of the Institute of Nuclear and Energy Technology. Karlsruhe: Scientific Publishing KIT; 2015. doi:10.5445/KSP/1000057984.
- Herzberger P, Münch W, Kölbl T, Bruchmann U, Schlagermann P, Hötzl H, Wolf L, Rettenmaier D, Steger H, Zorn R, Seibt P, Möllmann GU, Sauter M, Ghergut J, Ptak T. The geothermal power plant Bruchsal. In: Proceedings world geothermal congress 2010, Indonesia, Bali. 25–29 April 2010. 2010.
- Hirsch A. Gesteinsuntersuchungen und Bausteinkartierung am Turmhelm des Freiburger Münsters. Diploma Thesis. Albert-Ludwigs-University Freiburg. 2008.
- Kaufmann-Knoke R. Zur Problematik von Mineralausfällungen insbesondere von (Ba,Sr) SO₄-Mischkristallen bei der Erdölförderung, Berichte Geolog.-Paläont. Institut, Christian-Albrechts-Universität Kiel. 1992.
- Konrad-Zuse Zentrum für Informationstechnik Berlin (ZIB). Avizo 9, Avizo users guide, FEI. 2016. p. 850.
- Klotz D, Lang H, Moser H, Behrens H. Ausbreitung von Radionukliden der Elemente I, Sr, Cs und Ce in oberflächennahen Lockergesteinen, GSF Bericht R 289, Gesellschaft für Strahlen- und Umweltforschung mbH, 84 Seiten, München. 1982.
- Kühn M, Vernoux J-F, Kellner T, Isenbeck-Schröter M, Schulz HD. Onsite experimental simulation of brine injection into a clastic reservoir applied to geothermal exploitation in Germany. *Appl Geochem*. 1998;13(4):477–90.
- Merkel BJ, Planer-Friedrich B. Grundwasserchemie: Praxisorientierter Leitfaden zur numerischen Modellierung von Beschaffenheit, Kontamination und Sanierung aquatischer Systeme. Berlin: Springer Verlag; 2008.
- Ochi J, Vernoux J-F. Permeability decrease in sandstone reservoirs by fluid injection hydrodynamic and chemical effects. *J Hydrogeol*. 1998;208:237–48.
- Parkhurst DL, Appelo CAJ. Description of input and examples for PHREEQC version 3: a computer program for speciation, batch-reaction, one-dimensional transport, and inverse geochemical calculations. U.S. geological survey techniques and Methods, book 6, chapter A 43: Denver. 2013.
- Pauwels H, Fouillac C, Fouillac A-M. Chemistry and isotopes of deep geothermal saline fluids in the Upper Rhine Graben: origin of compounds and water-rock interactions. *Geochim Cosmochim Acta*. 1993;57:2737–49.
- Rosenbrand E, Kjoller C, Riis JF, Kets F, Fabricius IL. Different effects of temperature and salinity on permeability reduction by fines migration in Berea sandstone. *Geothermics*. 2015;53:225–35.
- Rosenbrand E, Haugwitz C, Munch Jacobsen PS, Kjoller C, Fabricius IL. The effect of hot water injection on sandstone permeability. *Geothermics*. 2014;50:155–66.
- Ruiz-Agudo C, Putnis CV, Ruiz-Agudo E, Putnis A. The influence of pH on barite nucleation and growth. *Chem Geol*. 2015;391:7–18.
- Sanjuan B, Millot R, Dezayes C, Brach M. Main characteristics of the deep geothermal brine (5km) at Soultz-sous-Forêts (France) determined using geochemical and tracer data. *C R Geosci*. 2010;342:546–59.
- Savage D, Bateman K, Richards HG. Granite-water interactions in a flow-through experimental system with applications to the hot dry rock geothermal system at Rosemanowes, Cornwall, U.K. *Appl Geochem*. 1992;7:223–41.
- Scheiber J, Seibt A, Birner J, Cuenot N, Genter A, Moeckes W. Barite scale control at the Soultz-sous-Forêts (France) EGS site. In: Proceedings, 38 workshop on geothermal reservoir engineering, Stanford University, Stanford, California. 24–26 February 2014. 2014.
- Schmidt RB, Bucher K, Drüppel K, Stober I. Experimental interaction of hydrothermal Na-Cl solution with fracture surfaces of geothermal reservoir sandstone of the Upper Rhine Graben. *Appl Geochem*. 2017;81:36–52.
- Soni JP, Islam N, Basak P. An experimental evaluation of non-Darcian flow in porous media. *J Hydrogeol*. 1978;38:231–41.
- Stober I, Bucher K. *Geothermie*. Heidelberg: Springer; 2012.
- Tutolo BM, Luhmann AJ, Kong X, Saar MO, Seyfried WE. CO₂ sequestration in feldspar-rich sandstone: coupled evolution of fluid chemistry, mineral reaction rates, and hydrogeochemical properties. *Geochim Cosmochim Acta*. 2015;160:132–54.

Submit your manuscript to a SpringerOpen[®] journal and benefit from:

- Convenient online submission
- Rigorous peer review
- Open access: articles freely available online
- High visibility within the field
- Retaining the copyright to your article

Submit your next manuscript at ► springeropen.com
